Ionic liquid gating induced insulating phase transition in $LaNiO_3$ thin films

Richmond Wang[1,2], Jihun Park[1,2], Rohit Pant[1,2], Suraj Maurya[1], Saya Takeuchi[1,3], Ichiro Takeuchi[1,2], and You Zhou[1,2]

[1]Department of Materials Science and Engineering, University of Maryland, College Park, MD 20742, USA;

[2]Maryland Quantum Materials Center, University of Maryland, College Park, MD 20742, USA;

[3]National Institute of Standards and Technology, Gaithersburg, MD 20899, USA;

Abstract

Perovskite rare-earth nickelates exhibit intriguing electrical and optical properties, such as metal-to-insulator transitions, resulting from the strong interplay between orbital order and electron correlation. Of these materials, lanthanum nickelate, $LaNiO_3$, is the only exception where the metallic phase is robust at all temperatures. Recently, significant efforts have been made to induce an insulating phase in $LaNiO_3$ by dimensionality or stoichiometry control. Electrolyte gating can be an efficient alternative to manipulate such electronic behavior reversibly and controllably. In this work, we performed systematic ionic liquid gating studies with electric double-layer transistor devices to control the electronic properties of $LaNiO_3$. The electrolyte gating in $LaNiO_3$ leads to an insulating phase transition with an increased film resistivity by over six orders of magnitude. The electrolyte gating behaviors are found to be dependent on not only gating voltage and duration, but also the atmospheric environment and temperature. X-ray photoelectron spectroscopy analysis reveals that the ionic liquid gating changes the O vacancy concentration and Ni valence state with varying gating times. The phase transition is attributed to enhanced electron correlation as well as opening of the charge transfer gap due to the reduced overlap between Ni and O bands. Intriguingly the filling of carriers into the Mott-Hubbard gap vs. charge transfer gap is controlled by the gate voltage. These results suggest that electrolyte gating devices can be useful for manipulating electron-electron correlation, boosting materials research to realize exotic physics in correlated systems.

Introduction

Transition-metal oxides exhibit a wide range of intriguing electrical and optical properties, with one such example being perovskite rare-earth nickelates ($RNiO_3$ where R = rare-earth metal). One specific property of the $RNiO_3$ materials is a metal-to-insulator transition (MIT), where the material transitions from a metallic phase to an insulating phase due to strong interplay electron correlation and orbital ordering[1–3]. The phase transition temperature, T_{MI}, increases with decreasing cation size of the rare-earth element which reduces the Ni–O–Ni bond angle[4,5].

The metallic phase in these $RNiO_3$ materials originates from the hybridization of the Ni *3d* and O *2p* bands[4,6–8]. The mechanism for stabilizing the insulating phase at low temperatures in $RNiO_3$ has been attributed to charge disproportionation among Ni sites, wherein the bandgap opened by the charge disproportionation [4,7–11] is strongly influenced by the Ni–O–Ni bond angle[4,6].

In addition to thermal phase transitions, the electronic structures of such oxides can also be modified by methods including strain engineering[6,12–14], cation substitution[15], or oxygen vacancy control [5,16–18]. Of particular interest is the control of $LaNiO_3$, the only rare-earth nickelate that is metallic at all temperatures in its bulk form[4,5,17,19]. In particular, vacuum annealing[7,17] and dimensionality control of $LaNiO_3$ films[19] have been explored as novel methods to generate oxygen vacancies and induce an insulating phase in the metallic compound.

In this paper, we explore a method for reliably and reproducibly altering the electrical properties of $LaNiO_3$ through ionic liquid (IL) gating[20–24]. IL gating utilizes an electric double-layer transistor (EDLT) structure to manipulate the charge carrier density in a material, as shown in Figure 1c[25]. In an EDLT, a gate voltage (V_G) is applied between an IL and a target material, such as $LaNiO_3$. At small voltages, the mobile ions moving under the V_G are unable to permeate into the sample and accumulate near the film surface[26]. This induces an equal charge density on the sample side of the interface, resulting in electrostatic doping of carriers. Under large enough bias, ions can pass through the surface of the sample through an electrochemical process and generate interstitials, substitutional defects, or vacancies in the films[25–27]. Such electrochemical processes lead to drastic and nonvolatile changes in the sample's resistance and have been explored as a novel basis for neuromorphic computing[28–30].

In this study, we utilized electrolyte gating with ILs to control the electronic behavior of $LaNiO_3$ thin films. These electrolyte gated $LaNiO_3$ films exhibited a significant increase in resistivity, accompanying a transition from metallic to insulating behavior. We systematically investigated the resistance change depending on the IL gating voltage, gating environment, and duration. We observed non-trivial evolution of the Ni valence state and oxygen vacancy content using X-ray photoelectron spectroscopy (XPS), which were attributed to the competition between Mott-Hubbard band and charge-transfer gap. Our studies show that oxygen deficient nickelate thin films form a platform for investigating the interplay between correlation and charge transfer and electrolyte gating creates exciting avenues for the in-situ control of this interplay.

Experiment

Thin Film Growth

$LaNiO_3$ films were grown on single-crystalline $SrTiO_3$ (001) substrates by pulsed laser deposition. One-inch diameter $LaNiO_3$ targets (Lesker) were ablated with a KrF excimer laser (wavelength = 248 nm). $SrTiO_3$ substrates were pre-annealed at 930 ℃ with an oxygen partial pressure of 5 x 10^{-6} Torr in order to obtain atomically flat surfaces. For the depositions, the substrate temperature was kept at 570 ℃ with an oxygen partial pressure of 150 mTorr. The laser fluence used was 1 J/cm^2 with a laser repetition of 6 Hz.

Thin Film Characterization

The crystal structure and surface morphology of $LaNiO_3$ samples were characterized using X-ray diffraction (XRD) and atomic force microscopy (AFM), respectively. XRD measurements were performed using a Bruker D8 Advance. AFM measurements were performed using a Digital Instruments Nanoscope V AFM. To analyze the thickness of $LaNiO_3$ thin films, X-ray reflectometry (XRR) measurement was performed using the Bruker D8 Advance and analyzed by a LEPTOS software package.

Ionic Liquid Gating

A schematic view of the ionic liquid gating device is shown in Fig. 1(c). IL gating of the $LaNiO_3$ films was performed in two environments: in-air and in-vacuum. In-air measurements were performed in the ambient atmosphere using a probe station. Cr/Au contacts were deposited onto $LaNiO_3$ films using thermal evaporation with shadow masks. During the gating measurements, the films were immersed in the ionic liquid, 1-Hexyl-3-methylimidazolium bis(trifluoromethylsulfonyl)imide (HMIM-TFSI), and a third platinum probe was used as the gate electrode for the measurements. The resistivity of the sample is calibrated with 4-probe measurements in a van der Pauw geometry.

In-vacuum measurements were performed on prepared samples using a 9T PPMS system (Quantum Design). The vacuum level during the gating and measurement was kept at ~10 Torr. Samples used for PPMS gating measurements only had the $LaNiO_3$ film deposited on half of a 5 × 10 mm^2 $SrTiO_3$ substrate, leaving a 5 × 5 mm^2 section of the substrate exposed. Cr/Au contacts were again deposited using thermal evaporation and metal masks. In this case, another Cr/Au contact was deposited on the exposed substrate to serve as the gate electrode. Al wire bonding was used to connect the samples with the PPMS puck. Each sample was covered completely with the IL HMIM-TFSI before being inserted into the 9T PPMS. Two Keithley 2400 SourceMeter SMU units were used to measure the resistance of the films and apply V_G, simultaneously.

Electrochemical analysis

XPS measurements were performed at the National Institute of Standards and Technology with a Kratos XPS, using a monochromatic Al Kα (1486.6 eV) X-ray source. Analysis of the data was performed using CasaXPS. A Shirley background method was used and each spectrum was calibrated based on the carbon peaks at 284.8 eV as the reference peak[31].

Results

Figure 1a shows the pseudo-cubic crystal structure of $LaNiO_3$ thin films. The XRD patterns of the $LaNiO_3$ thin films were measured to characterize the crystal structure and quality of the film. The XRD patterns of the pristine films show the presence of a diffraction peak maximum at around 47.9° alongside the $SrTiO_3$ substrate peak, as seen in Figure 1b. This confirms the successful deposition of pristine $LaNiO_3$ on the $SrTiO_3$ substrate without detectable impurity phases. The XRR measurements seen in Figure 1b inset showed that the films were approximately 35 nm thick. The initial temperature-dependent resistivity of the films measured using a 9T PPMS showed metallic behavior, as seen in Figure 1d.

We first investigate the modification of the LNO resistivity with varying gate voltage V_G at room temperature in air. We first apply a small gate voltage of +1V to the sample and observe an increase of the sample's resistivity from its initial value of around 129.4 nΩ cm to 130.7 nΩ cm. Even under a small gate voltage, we note obvious hysteretic gating behaviors. When the gate voltage is removed, the sample resistivity drops but to a value higher than the pristine state. Under a negative voltage, the sample resistance returns to its initial state, and remains close to its value after the gate voltage is removed, suggesting the reversibility of the gating process under this particular gating cycle. This reversibility was measured with a different pristine sample and was repeatable, as shown in Figure 2b, where the resistivity stabilized at a similar level after each cycle.

The symmetric response to gate voltage is essential for applications in neuromorphic computing devices. To further investigate the film's response to such a gating procedure, we increase the maximum gating voltage to 3V. This cycle was then repeated with ±2V and ±3V, with the measured resistivities shown in Figure 2a. An applied V_G = +2V increases the resistivity from 129.4 to 173.2 nΩ cm, with a subsequent V_G = -2V reducing the resistivity to 152.4 nΩ cm. Once the V_G is removed, the resistivity stabilizes around 150 nΩ cm. For the maximum gate voltage of +3V, the resistivity increases up to 4,383 nΩ cm and stabilizes at 740.9 nΩ cm when the voltage is reversed to -3V after 15 minutes.

In contrast to low gate voltage, higher gate voltages ($|V_G| \geq$ 2V result in a net increase in the resistivity of the films. For a V_G = ±2V, the resistivity shits by ~0.02 mΩ cm, while a V_G =

±3V increases the resistivity by up to 30 times its initial state before it stabilizes at ~0.719 mΩ cm, five times larger than the initial resistivity.

The hysteretic gating behaviors at all gate voltages and modification of the sample's resistivity at higher gates suggest that electrochemical processes significantly contribute to the observed resistivity change. The fact that the sample's resistivity does not revert to its initial values under this symmetric gating procedure suggests asymmetric reaction barriers for electrochemical reactions during the ionic liquid gating experiments. To further understand the underlying electrochemical reactions, we perform IL gating measurements in different ambient conditions, i.e. air and vacuum, and measure the change in resistivity under +3V gate over long periods of time. As seen in Figure 2c, samples gated in-air show a peak resistivity of 211 mΩ cm, before stabilizing around 150 mΩ cm after four hours. In contrast, gating $LaNiO_3$ films in-vacuum results in an increase in resistivity from 0.08 to a peak of 65,500 mΩ cm, before stabilizing at around 46,000 mΩ cm after a period of four hours.

IL gating of the $LaNiO_3$ thin films results in not only an increase in the resistivity of the film, but also modifies the band structures of the sample. This is evidenced by the resistivity-temperature measurements taken using in-vacuum gated samples from 300K down to 1.8K. As seen in Figure 2d, pristine samples show metallic behavior, with decreasing resistivity as the temperature decreases. After a $LaNiO_3$ film sample was gated in vacuum for four hours and its resistivity had stabilized, the temperature was reduced to 1.8K with the IL and V_G still applied to the sample. Unlike the pristine $LaNiO_3$ sample, this gated sample with $V_G = +3V$ shows an insulating resistivity behavior, where the resistivity increased from 3,500 to over 42,000 mΩ cm as the temperature decreased. Interestingly, the insulating behavior persists even after removing the ionic liquid and the vacuum environment. After removing the sample from PPSM vacuum and rinsing with IPA to remove the IL, the samples were then stored in a desiccator for a few days before being remeasured in a PPMS. When the *R*–*T* behavior was remeasured, the initial resistivity at room temperature had reduced to 240 mΩ cm but showed an insulating behavior, demonstrating a persistent change in the electrical properties of the $LaNiO_3$ films compared to its initial pristine state. Remarkably, even very low gate voltage ($V_G << 1V$) can induce insulating behavior in the $LaNiO_3$ devices, making the slope of the *R*–*T* curve negative (Figure 2d).

AFM measurements of pristine and gated films reveal the changes in surface morphology in the $LaNiO_3$ films due to IL gating. Pristine films have a surface roughness (RMS) of around 0.83 nm, showing that the PLD process produced uniform and smooth films, seen in Figure 1d inset. Films that were gated at $V_G = +3V$ for over 10 hours show significantly increased surface roughness with an RMS value of 4.55 nm, demonstrating how the IL gating process affects the surface properties and can cause degradation in the $LaNiO_3$ films.

Commented [YZ1]: Please mention the thickness of the film. Is the film still continuous?

In order to investigate the underlying electrochemical reactions leading to our experimental observations, XPS measurements were taken on various films which were gated for different periods of time. XPS graphs of the O 1s and Ni 3*p* spectra for pristine and 40-hour gated films are shown in Figure 3. The XPS data were calibrated using the C 1*s* = 284.8 eV peak as a standard[31]. The O 1s spectra show peaks at 527.9 and 528.5 eV (O_{lat}), which can be attributed to lattice oxygens that are bonded to La and Ni atoms in the crystal structure, respectively [6,32–34]. The peak at around 531.2 eV (O_V) has been shown to be representative of oxygen vacancies that have formed in the film [6,32–35]. From the O 1s spectra with increasing gating time, the ratio O_V/O_{lat}, showing the concentration of oxygen vacancies in the film, can be determined. For pristine samples, O_V/O_{lat} is approximately 1.07. As the samples are gated for increasing periods of time, the ratio increases up to 2.58 for the 40-hour gated $LaNiO_3$ sample.

This suggests that the IL gating of the film results in an increased oxygen vacancy formation in the film. This also explains how the gating environment affects the sample's response to electrical voltages. In the in-air environment with high oxygen partial pressure, the IL contains more oxygen and in fact can be saturated with oxygen atoms[25]. This decelerates the process of removing the oxygen atoms from the $LaNiO_3$ films, reducing the amount of oxygen vacancies formed in the film and resulting in a smaller resistivity peak. In contrast, gating in-vacuum allows the oxygen atoms that are removed from the film to be purged from the vacuum chamber, resulting in more oxygen vacancies in the film and a greater change in resistivity[25,34].

The increased oxygen vacancy formation in the films can result in the reduction of Ni^{3+} to Ni^{2+} in the films, which we further investigated using the Ni 3p spectra, as shown in Figure 3. Due to the coupling of spin-orbit splitting and multi-splitting, both the La *3d* and Ni *2p* spectra show complex multi-component structures[15,36,37]. The Ni $2p_{3/2}$ peaks also overlap with the La $3d_{3/2}$ peaks, creating difficulties in determining the Ni valence in the films[38–40]. On the other hand, the Ni 3p core-level spectrum, while having a reduced intensity compared to the Ni *2p* spectrum, does not overlap with other peaks[17,38,41]. Therefore, the Ni 3p core-level spectrum was used to distinguish between Ni^{3+} and Ni^{2+} in the films. The Ni 3p spectrum shows peaks at 66.46 and 70.09 eV, corresponding to Ni^{3+} and Ni^{2+} $3p_{3/2}$, respectively, as well as their satellite peaks[17,35,38,41–43]. The pristine sample exhibits a Ni^{3+}/Ni^{2+} ratio of 0.304. The relatively high Ni2+ content in pristine samples could be related to the formation of oxygen vacancies at the sample surface due to the thermodynamic instability of Ni^{3+} ions[44]. As the films are gated for longer periods of time, this ratio decreases to 0.143, showing the shift in Ni valence in the film towards Ni^{2+}. These XPS measurements offer complementary insights into the trend where longer gating times increase the resistivity of the $LaNiO_3$ films, affecting the Ni valence and oxygen vacancy concentration.

Previous experiments established that in the absence of hydrogen doping, the IL-gated rare earth nickelate can go through the following electrochemical reactions[28]

$$2Ni^{3+} + O_O^X \leftrightarrow 2Ni^{2+} + V_O^{2+} + \frac{1}{2}O_2 \qquad (1)$$

When the oxygen leaves the nickelate lattice, the Ni^{3+} atoms in the lattice become destabilized and form Ni^{2+} ions, resulting in the increase in resistivity that is seen in the films[28]. This is consistent with our XPS studies of LaNiO3 films at the initial gating stage, where both Ni valence state and oxygen vacancy concentration are modified significantly, as shown in Fig. 4a. Intriguingly, with longer gating time, the change in the Ni valence slows down while the oxygen vacancy concentration shows a more significant increase. This suggests that a more complicated electrochemical process than previously assumed occurs over longer gating periods, where oxygen vacancies are created without significant modification of the formal Ni valance state.

To understand the observed experimental phenomena, we first rationalize the change in the resistivity and then examine additional insights gained from chemical characterizations. The change in electrical properties of the $LaNiO_3$ films can be attributed to the shifts in oxygen vacancy concentration and Ni valence in the films. The metallic behavior in $LaNiO_3$ comes from the overlap between the occupied O *2p* valence band and the unoccupied Ni *3d* conduction bands[38]. When oxygen vacancies are introduced into the film, the Ni valence shifts from Ni^{3+} to Ni^{2+}. Compared with Ni^{3+} with a $(t_{2g}^6 e_g^1)$ electron configuration, Ni^{2+} hosts a partially filled e_g orbital $(t_{2g}^6 e_g^2)$ at exactly half-filling, which leads to much stronger correlated electron effects and leads to a bandgap in the film [7,16,18,34,45]. Furthermore, the larger ionic radius of Ni^{2+} (69 pm) compared to Ni^{3+} (56 pm) increases the Ni–O bond length and reduces the Ni–O–Ni bond angle[34,46]. This causes a reduction in the bandwidth for both the O *2p* and Ni *3d* bands and reduces the overlap. The reduction of the bandwidth also opens up a larger charge transfer bandgap, as shown in Figure 4[7,33,41,42]. These effects of the Ni valence change result in the bandgap opening and lead to the increased resistivity exhibited by the films, i.e., a transition from a metallic phase to an insulating phase in $LaNiO_3$.

While this simple picture captures the essence of the experimental observations, the evolution of oxygen vacancy concentrations and Ni valence states from XPS analysis reveals the nontrivial band hybridization effects. In particular, for short gating duration and low oxygen vacancy concentrations, there is a large modification of the formal valence state of Ni, indicating that a significant fraction of electrons is added to nickel with positively charged oxygen vacancy formation, as shown in equation (1). Upon higher doping concentrations, the removal of oxygen vacancies does not modify the Ni valence state at the same rate as before (Figure 4a), suggesting the electrons now occupy the oxygen vacancy sites by creating vacancies with reduced positive charges V_O^+ or even neutral charges V_O^O. In the band structure picture, this corresponds to the electron filling of the O 2p band. Therefore, the insulating states created by the ionic liquid gating at the longer gating period shall be considered as an intermediate state between Mott-Hubbard and charge-transfer insulator featuring significant band overlap between the O 2p band and the upper Hubbard band. Such realization of a mixed Mott-Hubbard and charge-transfer state creates exciting opportunities for investigating and controlling the interplay between correlation and charge-transfer in oxides by ionic liquid gating.

As the changes in resistivity can be attributed to an increased concentration of oxygen vacancies and a Ni valence change, it is possible that the MIT in $LaNiO_3$ that occurs due to the applied positive V_G can be reversed by switching the polarity of the applied gate voltage. We note, however, that in our symmetric gating experiments the resistivity increases to a higher value than its initial state. In rare earth nickelates, Ni^{2+} is known to be thermodynamically more favorable than Ni^{3+} under ambient oxygen pressures. Although Ni^{3+} in LNO is the most stable among the rare earth nickelate family[44], the thermodynamic and kinetic barriers to switch from Ni^{3+} to Ni^{2+} can be still considerably smaller than the reversal process. For applications in neuromorphic computing, it is critical to have a pair of bistable states with minimal difference in the thermodynamic and kinetic barriers so that one can realize a symmetric gate response[28,47,48]. Further development of methods to control the energy landscapes such as by strain tuning[49,50] and capping with an oxygen barrier to prevent oxygen[51–54] loss to the environment could open exciting avenues for applications to neuromorphic computing devices.

Conclusion

We fabricated $LaNiO_3$ thin films using PLD and performed systematic IL gating experiments by tuning gate voltage, duration, and vacuum environment. We observed an increase in the resistivity over six orders of magnitude in the $LaNiO_3$ devices gated in a low vacuum. This is attributed to a rise in oxygen vacancy concentration and a shift in the Ni valence from Ni^{3+} to Ni^{2+}. XPS analysis further shows non-trivial modification of Ni and O valence states, which were attributed to the electron filling of the Mott-Hubbard and charge-transfer bands. These electrochemical transitions enhance electron-electron correlation, thus decreasing bandwidth, reducing the overlap between O and Ni bands, and eventually inducing an insulating phase transition in $LaNiO_3$. This demonstrated capability of reliably and reversibly manipulating the electrical properties of perovskite nickelate thin films via IL gating opens new avenues for investigating the interplay between electron correlation and orbital effects and may find applications in neuromorphic computing.

Acknowledgements

This work was supported by ONR MURI (Award No. N00014-17-1-2661) and AFOSR FA9950-22-1-0023. S.M. and Y.Z. acknowledge support from the National Science Foundation (NSF) CAREER Award under Award No. DMR-2145712.

References

1. Stewart, M. K., Liu, J., Kareev, M., Chakhalian, J. & Basov, D. N. Mott Physics near the Insulator-To-Metal Transition in NdNiO 3. (2011) doi:10.1103/PhysRevLett.107.176401.

2. Middey, S. *et al.* Physics of Ultrathin Films and Heterostructures of Rare-Earth Nickelates. *https://doi.org/10.1146/annurev-matsci-070115-032057* **46**, 305–334 (2016).

3. Chakhalian, J. *et al.* Orbital reconstruction and covalent bonding at an oxide interface. *Science (1979)* **318**, 1114–1117 (2007).

4. Catalano, S. *et al.* Rare-earth nickelatesRNiO3: thin films and heterostructures. *Rep. Prog. Phys.* **81**, 46501 (2018).

5. Liao, X., Singh, V. & Park, H. Oxygen vacancy induced site-selective Mott transition in LaNiO 3. *Phys. Rev. B.* **103**, (2021).

6. Zhu, M. W. *et al.* Strain-induced modification in microstructure and electrical properties of polycrystalline LaNiO3−δ films. *Appl Phys A Mater Sci Process* **122**, 1–7 (2016).

7. Wang, L. *et al.* Oxygen Vacancy Induced Room-Temperature Metal-Insulator Transition in Nickelate Films and Its Potential Application in Photovoltaics. *ACS Appl Mater Interfaces* **8**, 9769–9776 (2016).

8. Liu, J. *et al.* Heterointerface engineered electronic and magnetic phases of NdNiO3 thin films. *Nature Communications 2013 4:1* **4**, 1–11 (2013).

9. Allen, S. J. *et al.* Gaps and pseudogaps in perovskite rare earth nickelates. *APL Mater* **3**, 062503 (2015).

10. Bisogni, V. *et al.* Ground-state oxygen holes and the metal–insulator transition in the negative charge-transfer rare-earth nickelates. *Nature Communications 2016 7:1* **7**, 1–8 (2016).

11. Green, R. J., Haverkort, M. W. & Sawatzky, G. A. Bond disproportionation and dynamical charge fluctuations in the perovskite rare-earth nickelates. *Phys Rev B* **94**, 195127 (2016).

12. Sidik, U. *et al.* Tunable Proton Diffusion in NdNiO3 Thin Films under Regulated Lattice Strains. *ACS Appl Electron Mater* (2022) doi:10.1021/ACSAELM.2C00711.

13. Aydogdu, G. H., Ha, S. D., Viswanath, B. & Ramanathan, S. Epitaxy, strain, and composition effects on metal-insulator transition characteristics of SmNiO3 thin films. *J Appl Phys* **109**, 124110 (2011).

14. Torriss, B., Margot, J. & Chaker, M. Metal-Insulator Transition of strained SmNiO3 Thin Films: Structural, Electrical and Optical Properties. *Scientific Reports 2017 7:1* **7**, 1–9 (2017).

15. Amarasinghe, D. K. *et al.* Electron doping of NdNiO3 thin films using dual chamber CaH2 annealing. *J Solid State Chem* **315**, 123512 (2022).

16. Lin, H., Jakub Gawryluk, D., Maximilian Klein, Y. & Lechermann, F. Assessing the correlated electronic structure of lanthanum nickelates. *Electronic Structure* **4**, 015005 (2022).

17. Wong, J. C. *et al.* Understanding the Role of Defective Phases on the Conductivity Behavior of Strained Epitaxial LaNiO3Thin Films. *ACS Appl Electron Mater* **4**, 1196–1205 (2022).

18. Li, J., Ramanathan, S. & Comin, R. Carrier Doping Physics of Rare Earth Perovskite Nickelates RENiO3. *Front Phys* **10**, 33 (2022).

19. Golalikhani, M. *et al.* Nature of the metal-insulator transition in few-unit-cell-thick LaNiO3 films. *Nature Communications 2018 9:1* **9**, 1–8 (2018).

20. Dong, Y. *et al.* Effect of gate voltage polarity on the ionic liquid gating behavior of NdNiO3/NdGaO3 heterostructures. *APL Mater* **5**, 051101 (2017).

21. Maruyama, S. *et al.* Reversible electrochemical modulation of the superconducting transition temperature of LiTi2O4 ultrathin films by ionic liquid gating. *Appl Phys Lett* **107**, 142602 (2015).

22. Leighton, C. Electrolyte-based ionic control of functional oxides. *Nature Materials 2018 18:1* **18**, 13–18 (2018).

23. Asanuma, S. *et al.* Tuning of the metal-insulator transition in electrolyte-gated NdNiO3 thin films. *Appl Phys Lett* **97**, 142110 (2010).

24. Ha, S. D., Vetter, U., Shi, J. & Ramanathan, S. Electrostatic gating of metallic and insulating phases in SmNiO3 ultrathin films. *Appl Phys Lett* **102**, 183102 (2013).

25. Kalhori, H. *et al.* Oxygen Vacancy in WO3 Film-based FET with Ionic Liquid Gating. *Scientific Reports 2017 7:1* **7**, 1–10 (2017).

26. Walter, J., Wang, H., Luo, B., Frisbie, C. D. & Leighton, C. Electrostatic versus Electrochemical Doping and Control of Ferromagnetism in Ion-Gel-Gated Ultrathin La0.5Sr0.5CoO3-δ. *ACS Nano* **10**, 7799–7810 (2016).

27. Ueno, K., Shimotani, H., Iwasa, Y. & Kawasaki, M. Electrostatic charge accumulation versus electrochemical doping in SrTiO3 electric double layer transistors. *Appl Phys Lett* **96**, 252107 (2010).

28. Shi, J., Ha, S. D., Zhou, Y., Schoofs, F. & Ramanathan, S. A correlated nickelate synaptic transistor. *Nat Commun* **4**, 2676 (2013).

29. Ohno, T. *et al.* Short-term plasticity and long-term potentiation mimicked in single inorganic synapses. *Nat Mater* **10**, 591–595 (2011).

30. Raoux, S., Wełnic, W. & Lelmini, D. Phase change materials and their application to nonvolatile memories. *Chem Rev* **110**, 240–267 (2010).

31. Fang, D., He, F., Xie, J. & Xue, L. Calibration of Binding Energy Positions with C1s for XPS Results. *Journal Wuhan University of Technology, Materials Science Edition* **35**, 711–718 (2020).

32. Li, P., Tian, C., Yang, W., Zhao, W. & Lü, Z. LaNiO3 modified with Ag nanoparticles as an efficient bifunctional electrocatalyst for rechargeable zinc–air batteries. *Front Mater Sci* **13**, 277–287 (2019).

33. Fu, Y. *et al.* Core-level x-ray photoemission and Raman spectroscopy studies on electronic structures in Mott-Hubbard type nickelate oxide NdNiO 2. (2020).

34. Anjeline, C. J., Marate, B. G., Velu, D., Kumar, S. M. S. & Lakshminarasimhan, N. Probing oxygen vacancy-induced mixed-valence states of nickel in LaNiO3 and their influence on electrocatalytic and magnetic properties. *Mater Chem Phys* **288**, 126331 (2022).

35. Wang, Y. *et al.* Promoting the Oxygen Evolution Activity of Perovskite Nickelates through Phase Engineering. *ACS Appl Mater Interfaces* **13**, 58566–58575 (2021).

36. Carley, A. F., Chalker, P. R. & Roberts, M. W. Defects in Oxide Overlayers at Nickel Single-Crystal Surfaces. *Source: Proceedings of the Royal Society of London. Series A* **399**, 167–179 (1985).

37. Dubey, P., Kaurav, N., Devan, R. S., Okram, G. S. & Kuo, Y. K. The effect of stoichiometry on the structural, thermal and electronic properties of thermally decomposed nickel oxide †. (2018) doi:10.1039/c8ra00157j.

38. Qiao, L. & Bi, X. Direct observation of Ni3+ and Ni2+ in correlated LaNiO3−δ films. *Europhys Lett* **93**, 57002 (2011).

39. Mickevičius, S. *et al.* Investigation of epitaxial LaNiO3−x thin films by high-energy XPS. *J Alloys Compd* **423**, 107–111 (2006).

40. Maluf, S. S., Tanabe, E. Y., Nascente, P. A. P. & Assaf, E. M. Study of water-gas-shift reaction over La(1-y)Sr yNixCo(1-x)O3 perovskite as precursors. *Top Catal* **54**, 210–218 (2011).

41. Hien-Hoang, V., Chung, N. K. & Kim, H. J. Electrical transport properties and Kondo effect in La 1−x Pr x NiO 3−δ thin films. *Scientific Reports 2021 11:1* **11**, 1–10 (2021).

42. Burriel, M. *et al.* Absence of Ni on the outer surface of Sr doped La 2 NiO 4 single crystals. *Energy Environ Sci* **7**, 311–316 (2013).

43. McBean, C. L. *et al.* Generalizable, Electroless, Template-Assisted Synthesis and Electrocatalytic Mechanistic Understanding of Perovskite LaNiO3 Nanorods as Viable, Supportless Oxygen Evolution Reaction Catalysts in Alkaline Media. *ACS Appl Mater Interfaces* **9**, 24634–24648 (2017).

44. Jaramillo, R., Schoofs, F., Ha, S. D. & Ramanathan, S. High pressure synthesis of SmNiO 3 thin films and implications for thermodynamics of the nickelates. *J Mater Chem C Mater* **1**, 2455–2462 (2013).

45. Shin, Y. & Rondinelli, J. M. Magnetic structure of oxygen-deficient perovskite nickelates with ordered vacancies. *Phys Rev Res* **4**, 22069 (2069).

46. Shannon, R. D. Revised effective ionic radii and systematic studies of interatomic distances in halides and chalcogenides. *Acta Crystallographica Section A* **32**, 751–767 (1976).

47. Van De Burgt, Y., Melianas, A., Keene, S. T., Malliaras, G. & Salleo, A. Organic electronics for neuromorphic computing. *Nature Electronics 2018 1:7* **1**, 386–397 (2018).

48. Christensen, D. V. *et al.* 2022 roadmap on neuromorphic computing and engineering. *Neuromorphic Computing and Engineering* **2**, 022501 (2022).

49. Fowlie, J. *et al.* Conductivity and Local Structure of LaNiO3 Thin Films. *Advanced Materials* **29**, 1605197 (2017).

50. Ardizzone, I. *et al.* Optical properties of ${\rm La}{\rm Ni}{\rm O}_3$ films tuned from compressive to tensile strain. *Phys Rev B* **102**, 155148 (2020).

51. Salg, P. *et al.* Oxygen diffusion barriers for epitaxial thin-film heterostructures with highly conducting SrMoO3 electrodes. *J Appl Phys* **127**, 65302 (2020).

52. Detavernier, C., Van Meirhaeghe, R. L., Cardon, F., Donaton, R. A. & Maex, K. The influence of Ti capping layers on CoSi2 formation. *Microelectronic Engineering* **50**, 125–132 (2000).

53. Chen, B. *et al.* Influence of oxygen diffusion through capping layers of low work function metal gate electrodes. *IEEE Electron Device Letters* **27**, 228–230 (2006).

54. Bulusu, A., Kim, H., Samet, D. & Graham, S. Improving the stability of atomic layer deposited alumina films in aqueous environments with metal oxide capping layers. *J Phys D Appl Phys* **46**, 084014 (2013).

Figures

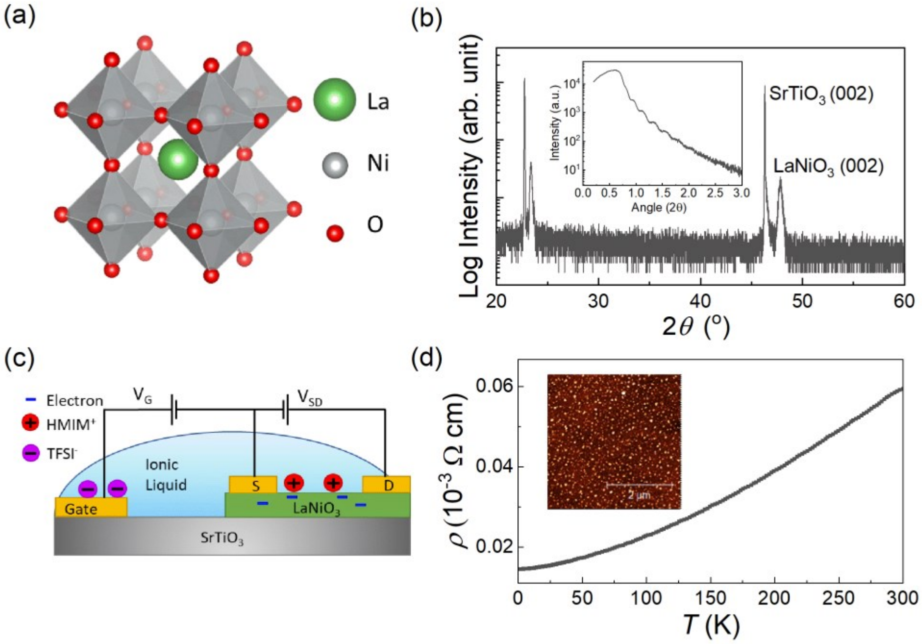

Figure 1. (a) Pseudo-cubic crystal structure of $LaNiO_3$ and (b) the XRD 2θ-ω scan of $LaNiO_3$ on $SrTiO_3$(001) substrates. Inset, XRR graph of $LaNiO_3$ films with thickness of 35 nm. (c) Side-view schematic of the IL-based electric double-layer transistor device used for the gating experiments. The ionic liquid used was HMIM-TFSI. S and D indicate source and drain electrodes, respectively. V_G indicates gate voltage applied, and V_{SD} indicates the applied source drain voltage used to measure the resistance of the films. (d) Temperature dependence of the resistivity of pristine $LaNiO_3$ thin films after PLD deposition. Inset, AFM image of pristine $LaNiO_3$ thin film with RMS value of 0.83 nm.

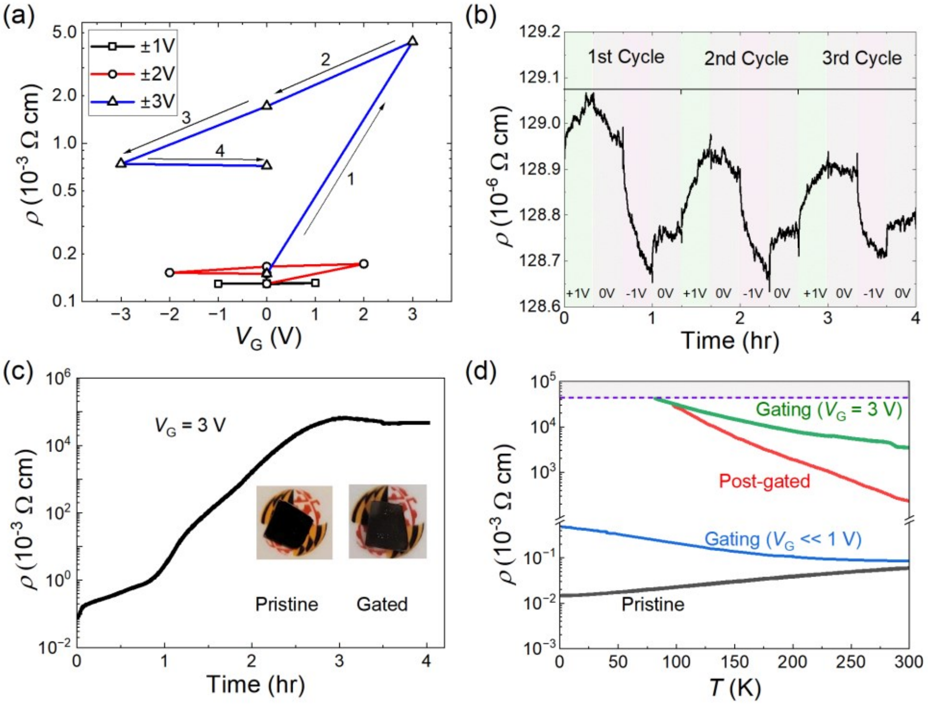

Figure 2. (a) Resistivity changes in $LaNiO_3$ with gate voltage cycling. The applied V_G sequence used: (1) 15 min positive V_G → (2) 15 min $V_G = 0V$ → (3)15 min negative V_G → (4) 15 min $V_G = 0V$. The voltages applied were $V_G = \pm 1V, \pm 2V$, and $\pm 3V$. (b) Reversibility of resistivity changes using a low applied $V_G = \pm 1V$. The cycles use the same sequence as before but for a duration of 20 minutes per segment. (c) Gating time dependence of room temperature resistivity in $LaNiO_3$ IL gating devices with a $V_G = + 3V$. Inset, images of pristine and gated samples showing color difference after IL gating. (d) Temperature dependence of $LaNiO_3$ samples in the pristine state (pristine), during IL gating (gating), and after the V_G and IL were removed from samples (post-gated). A physical measurement limit occurs when the resistance was too large to be measured (gray area).

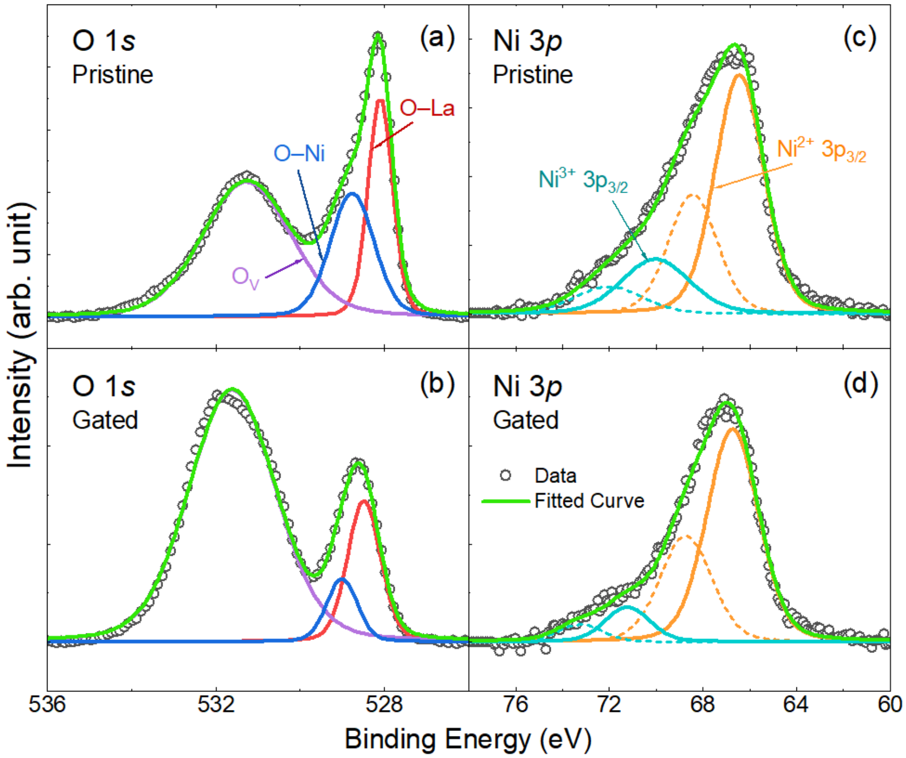

Figure 3. XPS spectra of $LaNiO_3$ films in pristine and gated states: O 1*s* for pristine (a) and gated (c) samples, and Ni 3*p* for pristine (b) and gated (d) samples. The O 1*s* XPS data was fitted by deconvoluting with three components: O–La (red), O–Ni (blue), O_V (purple). The Ni 3*p* XPS spectra show the deconvoluted $3p_{3/2}$ peaks (solid lines) and the $3p_{1/2}$ peaks (dashed lines) for Ni^{2+} (orange) and Ni^{3+} (cyan) ions.

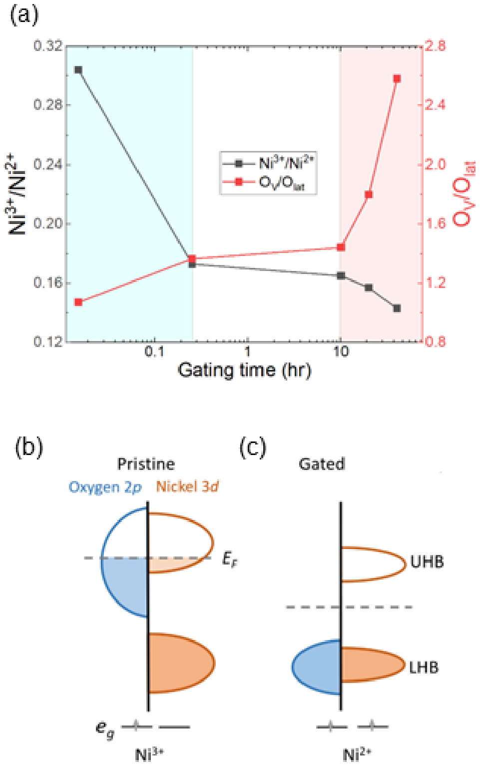

Figure 4. (a) Evolution of Ni valence state and oxygen vacancy concentration in $LaNiO_3$ as a function of IL gating time. The band structure and electron configuration of (b) pristine and (c) gated $LaNiO_3$.